Engineering Failure Analysis 138 (2022) 106354

Contents lists available at ScienceDirect

Engineering Failure Analysis

journal homepage: www.elsevier.com/locate/engfailanal

Fatigue fracture surface metrology of thin-walled tubular austenitic steel specimens after asynchronous loadings

Wojciech Macek [a,*], Łukasz Pejkowski [b], Ricardo Branco [c], Reza Masoudi Nejad [d], Krzysztof Żak [e]

[a] Gdańsk University of Technology, Faculty of Mechanical Engineering and Ship Technology, Gabriela Narutowicza11/12, 80-233 Gdańsk, Poland
[b] UTP University of Science and Technology in Bydgoszcz, Poland
[c] University of Coimbra, CEMMPRE, Department of Mechanical Engineering, Rua Luís Reis Santos, 3030-788 Coimbra, Portugal
[d] School of Mechanical and Electrical Engineering, University of Electronic Science and Technology of China, Chengdu 611731, China
[e] Opole University of Technology, Faculty of Mechanical Engineering, Mikołajczyka 5, 45-271 Opole, Poland

A R T I C L E I N F O

Keywords:
Multiaxial fatigue
Non-proportional loading
Austenitic steel
Fatigue life estimation
Fractography
Surface metrology

A B S T R A C T

This paper aims to study the effect of asynchronous axial-torsional strain-controlled loading histories on fracture surface behavior of thin-walled tubular X5CrNi18-10 (304/304L) austenitic steel specimens. Tests under pure axial loading and pure torsional loading are also conducted to better segregate the effect of multiaxiality. The fractures surface topographies were examined through the profiles over the entire surface with the support of an optical measurement system. Then, features of the post-failure fractures were related to the loading conditions and the fatigue life. The outcomes indicate that the multiaxial loading path significantly affects the surface topography. Overall, fracture surface parameters increase for higher fatigue lives. Based on the dialectic relationship, a fatigue damage model able to estimate the fatigue lifetime under asynchronous axial-torsional loading histories has been successfully developed. The fracture surface topology parameters collected from both sides of the same specimen lead to comparable results which reinforces the applicability of the proposed approach.

1. Introduction

Austenitic stainless steel is a material commonly used in engineering applications [1–5]. Thus, various austenitic steel grades are often mechanically tested, including fatigue and fracture tests. A few recent papers can be given as examples. Youn et al. studied the thermal aging effect on fracture toughness of gas-tungsten-arc-welded 316L steel [6]. Wu et al. [7] simulated crack extensions in 21-6-9 steel. Antunes et al. [8] used the plastic CTOD range parameter to investigate the crack propagation for the 304L steel. Nagaishi et al. performed fatigue tests on circumferentially-notched 304 steel specimens in air and in hydrogen atmosphere [9]. Jones et al. studied crack growth in specimens manufactured from 304L and 316L steel grades using two additive manufacturing techniques.

Since engineering parts and structures are often subjected to multiaxial loadings [10–13], many researchers study their effect on fatigue and fracture behavior [14–18], as well as the methods of fatigue life prediction [19–24]. One of the multiaxial loadings' features that gains particular interest is the non-proportionality of loading [25–28]. The reason is reduction of fatigue life compared to the proportional loadings [29] and other phenomena like additional hardening [30]. To study the effect of the non-proportional

* Corresponding author.
E-mail address: wojciech.macek@pg.edu.pl (W. Macek).

https://doi.org/10.1016/j.engfailanal.2022.106354
Received 16 March 2022; Received in revised form 21 April 2022; Accepted 21 April 2022
Available online 26 April 2022
1350-6307/

Nomenclature

Symbol	Description [Unit]
Δ	range of quantity [–]
ε	axial strain [mm/mm]
γ	shear strain [rad]
r	loading parameter [–]
λ	shear to normal strain ratio [–]
f_r	shear to normal strain frequency ratio [–]
N_f	number of cycles to failure [cycles]
λ_c	Gaussian cut-off filter length, wavelength to determine the bound between surface roughness component and waviness component [mm]
λ_s	Gaussian cut-off filter length, wavelength to determine the bound between surface roughness component and other shorter components [μm]
R_p	Maximum peak height of the roughness profile [μm]
R_v	Maximum valley depth of the roughness profile [μm]
R_z	Maximum height of roughness profile [μm]
R_c	Mean height of the roughness profile elements [μm]
R_t	Total height of roughness profile [μm]
R_a	Arithmetic mean deviation of the roughness profile [μm]
R_q	Root-mean-square (RMS) deviation of the roughness profile [μm]
R_{sk}	Skewness of the roughness profile [–]
R_{ku}	Kurtosis of the roughness profile [–]
R_{mr}	Relative material ratio of the roughness profile [%]
R_{dc}	Roughness profile section height difference [μm]
R^2	Proportion of the variance for a dependent variable [–]
Abbreviation	Description
TC	Tension-compression (axial loading)
TOR	Torsion
IP	in-phase proportional loading
OP	out-of-phase loading
ASNx	asynchronous loading, where x stands for a number denoting the number of loading path
MON	monotonic tension
SEM	scanning electron microscope
ISO	International Organization for Standardization
L	longer part of the broken specimen
S	shorter part of the broken specimen

loadings on the fatigue life, out-of-phase loadings are typically chosen [31–33]. However, non-proportional loadings may be more complicated. To investigate the influence of other non-proportional loading paths on fatigue behavior of metal alloys, Pejkowski et al. conducted experiments employing asynchronous loadings [34,35]. In case of these loadings, there is a difference in frequencies of strain components. Principal axes of stress and strain rotate, like in case of out-of-phase loadings, and the degree of non-proportionality differs. It was shown that the material response to asynchronous loadings is more complex, and fatigue life prediction is more challenging. The idea of including the asynchronous loadings in multiaxial fatigue testing campaigns was also used by other authors [36–39].

The fracture surface of materials has a complicated morphology [40,41]. For brittle materials, such as ceramic microstructure, more deflections are reasoned by the poor grain boundaries and therefore, the roughness of these fracture surfaces is increased [42]. Falkowska et al. [43] showed that the monotonic crack growth in sintered metal typically has a mixed ductile-brittle nature, which of course also has a great deal to do with the fracture surface topography. The research on the morphology of fatigue fractures is carried out on various scales (from macro to nano) and the most common fractographic studies are observations using SEM [44–46]. This method gives very good possibilities of qualitative description of the fracture. However, in order to quantitatively compare the fracture surface topology parameters associated with different materials or loading characteristics, metrological tools should be used [47–49].

Extracting fracture profile gives additional information about the failure process but requires post-failure analysis. Similar analysis were carried out by Macek et al. [50] who demonstrated a relationship between the strain sequence with the surface topography behavior. These promising results motivate the analysis of other materials subjected to different loading histories.

Although somes studies have addressed the correlation between the multiaxial proportional fatigue damage on fracture surface topology parameters, cases dealing with multiaxial asynchronous loading histories have not been reported yet. Thus, this paper addresses the effect of axial-torsional strain-controlled loading on fracture surface behavior in thin-walled tubular X5CrNi18-10 (304/304L) austenitic steel specimens. Tests under pure axial loading and pure torsional loading are also conducted to better understand the effect of multiaxiality. The fractures topographies are examined by taking into account the entire surfaces using an optical measurement system, and the different fracture surface parameters are related to the loading history and the associated fatigue life.

The present paper is organized as follows: Section 2 reports the materials and methods used for this investigation. Section 3 collects details on the experimental fatigue test and fractographic results. Section 4 presents the discussion and main results of the fatigue tests and the fracture profile parameters. The article finishes with a conclusion of the most relevant findings. In the end, Appendix A compiles the original area and profile for both sides of each specimen with a short table of results and the Abbott curve plots, respectively.

2. Materials and methods

2.1. Material and fatigue tests

Fatigue tests were performed during the experimental campaign described in [34]. Thin-walled specimens (see Fig. 1) were CNC machined from precise seamless pipes made of X5CrNi18-10 steel. All fatigue tests were conducted on an Instron 8874 servo-hydraulic

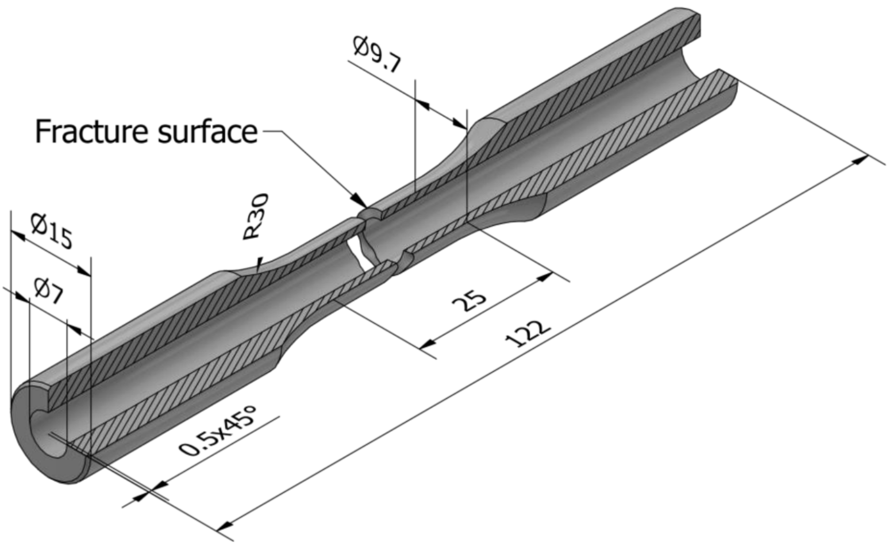

Fig. 1. Specimen shape and geometry (units: millimeters).

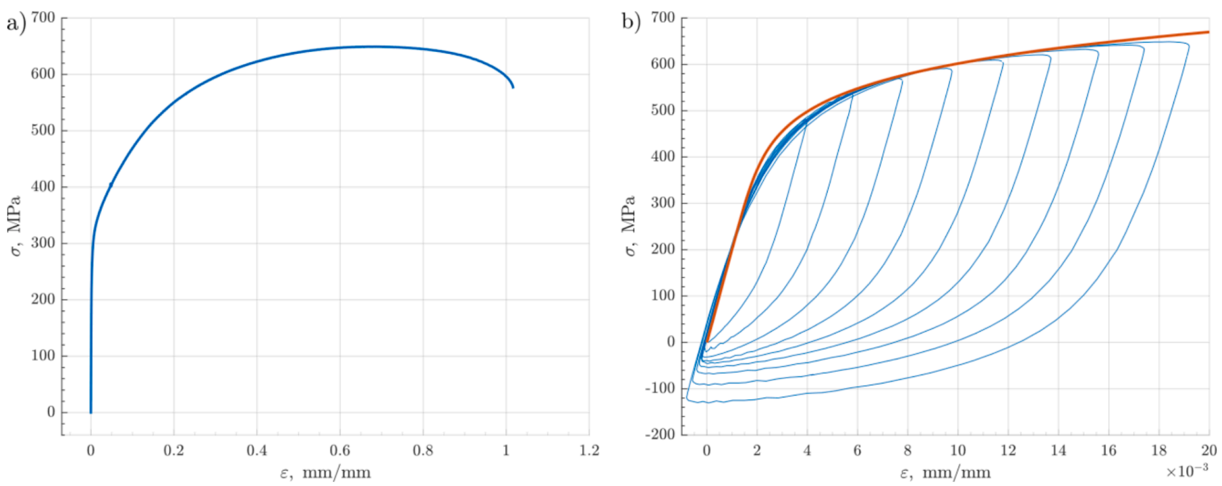

Fig. 2. a) Monotonic stress-strain curve, b) axial strain hysteresis loops with master curve.

Table 1
Basic mechanical properties of X5CrNi18-10 steel.

E, GPa	σ_{y02}, MPa	σ_u, MPa	ε_u, mm/mm	ν_e, –	K^*, MPa	n^*
200.8	265.0	645.4	0.687	0.29	1110.8	0.1235

system, equipped with an Epsilon 3550 biaxial extensometer. The frequency of fatigue tests varied to keep the maximum value of the equivalent Huber-Mises strain rate below 0.001 s^{-1}. Nine different loading cases were applied. The parameters of loadings are presented in Fig. 2, and some complementary information is provided in Table 2. Fully-reversed sine signals of axial $\varepsilon(t)$ and shear $\gamma(t)$ strains were applied:

$$\varepsilon(t) = \varepsilon_a \sin(2\pi f_\varepsilon t) \tag{1}$$

$$\gamma(t) = \gamma_a \sin\left(2\pi f_\gamma t + \delta\right) \tag{2}$$

where ε_a, γ_a, f_ε, f_γ are amplitudes and frequencies of normal and shear strain, respectively, and δ is a phase shift angle. The ratios of component strains amplitudes and frequencies are described by the coefficients $\lambda = \gamma_a/\varepsilon_a$ and $f_r = f_\gamma/f_\varepsilon$, respectively.

The basic mechanical properties of the tested austenitic steel, i.e. Young modulus E, offset yield stress σ_{y02}, ultimate tensile stress σ_u, total strain at failure ε_u, elastic Poisson ratio ν_e, strength parameter of master curve [51,52] K^*, and cyclic strain hardening exponent of Master curve n^* are listed in Table 1 [34]. Fig. 2 presents the monotonic tension stress-strain curve and the master curve determined based on the axial strain hysteresis loop.

Table 2
Summary of fatigue testing campaign.

Specimen	$\Delta\varepsilon/2$	$\Delta\gamma/2$	λ	f_γ/f_ε	$2N_f$, axial	$2N_f$, torsional	$2N_f$, path
029_TC	0.0055	0	0	1	3 758	0	3 758
009_TOR	0	0.0087	∞	1	0	32 305	32 305
037_PRO	0.0039	0.0067	$\sqrt{3}$	1	7 248	7 248	7 248
024_OOP	0.005	0.0087	$\sqrt{3}$	1	1 244	1 244	1 244
030_ASN1	0.0044	0.0076	$\sqrt{3}$	0.5	1 435	718	718
045_ASN2	0.0047	0.0041	$\sqrt{3}/2$	4	2 465	9 860	2 465
059_ASN3	0.0016	0.0054	$2\sqrt{3}$	0.2	107 312	21 462	21 462
058_ASN4	0.0048	0.005	$3\sqrt{3}/5$	6	1 866	11 196	1 866
066_ASN5	0.0039	0.0068	$\sqrt{3}$	0.7	3 011	2 108	301

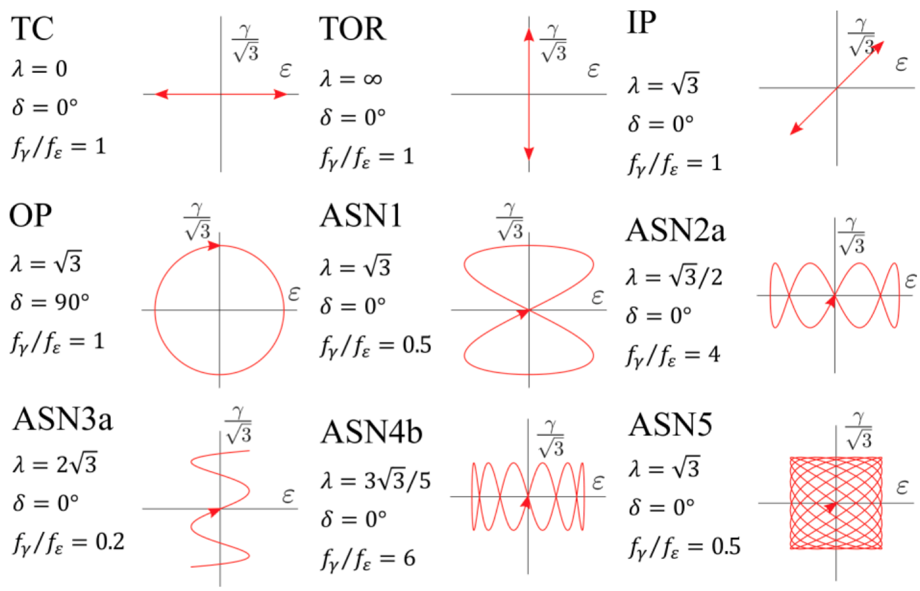

Fig. 3. Strain paths of applied loadings.

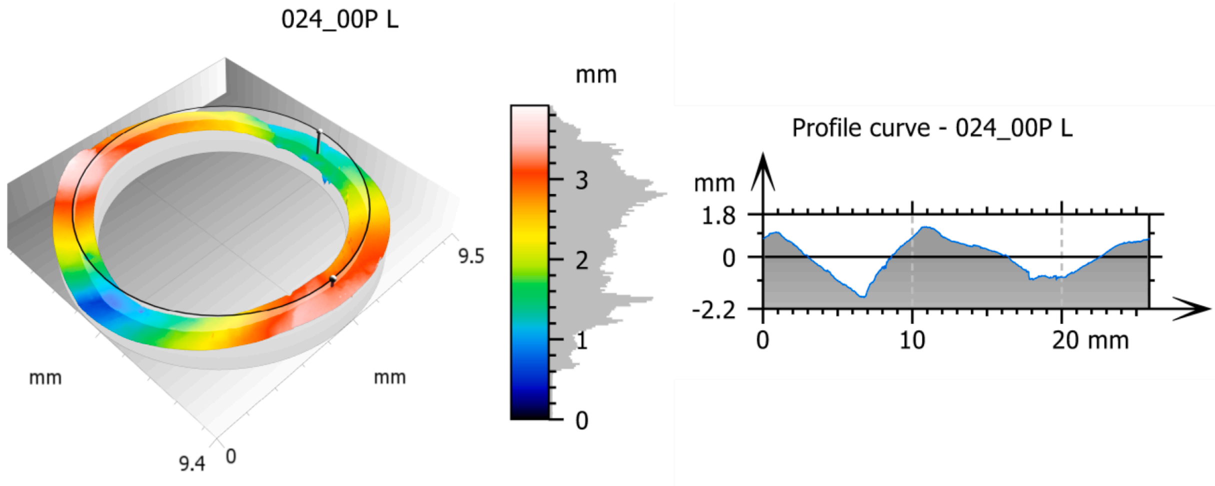

Fig. 4. Example of extracted profile.

2.2. *Fracture surface metrology*

A Sensofar S neox 3D optical surface metrology system was adopted to measure the fracture surface topography. The Focus Variation Method (FVM) was employed to determine the surface geometry of fractures, in the area of 9.09 × 9.36 mm^2 (3250 × 3391 pixels), with a pixel size of 2.76 μm/pixel. The lens used for the measurements is a Nikon EPI 5×.

In this study, a circular profile extraction was used (see Fig. 4). The profile of interest had a radius of 4.1 mm, generating profiles 25.76 mm long and with 18,667 points. Moreover, for confrontation, a specimen subjected to monotonic loading was checked, for which the extracted profile radius was 2.8 mm. Fig. 3 shows the 3D view of the 024_00P fracture surface (at the top of Fig. 4) and its profile curve (at the bottom of Fig. 4). Additionally, palette cursors and histogram are marked on the 3D view scale.

The extracted circle was selected at the middle of the fracture surface. In this specimen geometry the crack propagation is more stable in that region and therefore, it is simpler to capture the central part of the thin-walled tubular surface during the surface assessment which is likely to be more deformed. Thus, the center axis of the fracture surface is more representative of the studied specimen geometry. This arrangement of the measurement profiles also allows to avoid the non-measured points near the edges of measured surfaces.

3. Results

3.1. *Fatigue campaign results*

The fatigue lives obtained in the tests are listed in Table 2. Since in the case of the asynchronous loadings there is a difference in frequencies of the normal and shear strain waveforms, the fatigue life was given in terms of the axial and torsional loading cycles. It was also given as the number of strain path repetitions [34].

3.2. *Fracture surface topography analysis*

The fracture profile parameters are calculated and evaluated according to ISO 4287 [53–55] standard. The λ_s (Gaussian) filter, applied in the level 2.5 μm, removes scales smaller than the nesting index value of the filter. The λ_c filter (Gaussian) with a value of 0.8 mm that separates waviness from roughness was also applied. Evaluation length for all λ_c was 32. Fig. 5 shows an example of the original fracture profile and the same profile after filtering that was used to calculate the roughness parameters.

Based on the filtered profiles, the fracture surface profile measurement results are registered in Table 3 and are presented in Appendix A (see Fig. A1).

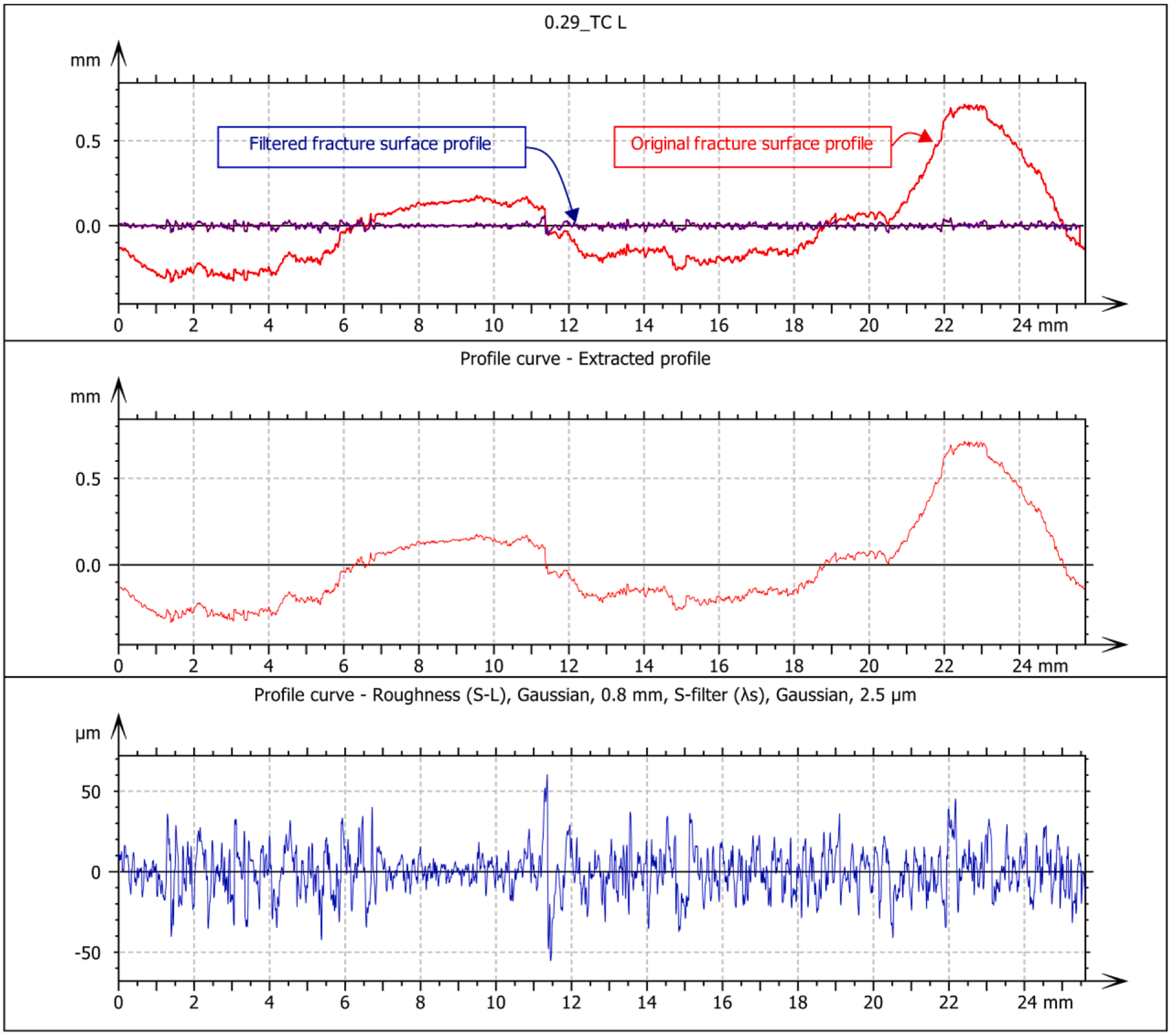

Fig. 5. Original and filtered fracture profile (roughness).

4. Discussion

4.1. Comparison of both sides of the specimen

Fig. 6 shows the surface profiles of fatigue fractures for the shorter and longer parts of the broken 0.29_TC specimen, for both the original and the filtered ones. The fact that one part is shorter and the other part is longer is a random phenomenon. The nomenclature “L” and “S” is adopted for easier identification of the samples.

An interesting subject that is not completely clear at this point is the reciprocity of the measured values of the two profiles of the fracture surface. This is due to the fact that the immediate part of the fatigue fracture deforms plastically, and then the fracture surfaces rub against each other as a result of the torsion component. Fig. 7 plots the most compatible values of profile roughness parameters for the long (L) side (horizontal axis) versus those for the short (S) side (vertical axis).

Fig. 8 compares the fracture surface parameters versus fatigue life expressed in reversals to failure. The results were further fitted with a power function:

$$R_{xx} = A\left(2N_f\right)^b \tag{3}$$

where R_{xx} is a roughness parameter, and A and b are fitting coefficients. Robust fitting, based on the bisquare weight function, was used in order to reduce the influence of the outliers. Observing the charts, it was noted that some of the roughness parameters correlate quite well with the fatigue life (R_a, R_z, R_q), while others do not (R_{qu}, R_{mr}, R_{sk}).

Table 3
Measured fracture surface profile parameters.

Specimen	R_p	R_v	R_z	R_c	R_t	R_a	R_q	R_{sk}	R_{ku}	R_{mr}	R_{dc}
029_TC L	26.9	28.19	55.09	31.94	115.6	10.52	12.89	−0.09	2.69	0.03	21.32
029_TC S	28.57	28.85	57.41	32.22	108.4	10.68	13.29	0.06	3.02	0.04	21.07
009_TOR L	132	118	250	492	2600	40.4	54.8	0.05	4.2	0.01	38.3
009_TOR S	125	119	244	327	1680	40.5	52.4	−0.09	3.56	0.01	38.2
037_PRO L	86.6	57.5	144	153	1170	23.3	31	0.275	4.96	0.00539	29.1
037_PRO S	144	53.9	198	648	2860	18.1	29.4	0.267	7.08	0.00539	27.2
024_OOP L	54.75	43.89	98.64	69.33	440.6	13.82	18.68	0.43	5.02	0.01	24.27
024_OOP S	49.98	35.83	85.81	82.08	681.1	11.53	16.15	0.14	4.4	0.01	20.21
030_ASN1 L	33.5	33.8	67.3	41.4	194	13	16.3	0.05	3.05	0.01	24.3
030_ASN1 S	37	38.9	75.9	48.3	282	12.7	16.5	−0.00285	3.66	0.01	22.6
045_ASN2 L	41.91	47.5	89.41	75.48	600.9	15.9	20.57	−0.02	2.94	0.01	23.58
045_ASN2 S	49.16	39.25	88.42	62.63	386.9	15.09	19.57	0.23	3.75	0.01	24.82
059_ASN3 L	30.1	30.5	60.6	36.4	294	8.56	11.6	−0.04	5.21	0.01	15.7
059_ASN3 S	23.06	26.2	50.1	29.5	159	7.48	9.88	−0.09	4.35	0.01	13.8
058_ASN4 L	65.84	61.6	127.4	92.92	594.4	15.45	22.72	0.06	6.31	0.01	25.49
058_ASN4 S	54.26	42.65	96.91	68.09	443.3	14.8	19.55	0.31	4.79	0.01	27.45
066_ASN5 L	21.1	27.9	49	28.1	202	7.48	9.86	−0.24	4.26	0.02	14.3
066_ASN5 S	19.6	21.3	41	23.9	128	7.2	9.09	−0.3	3.7	0.02	12.1
003_MON L	45.2	46.2	91.4	89.6	352	17.4	22.9	−0.07	3.01	0.03	22.6
003_MON S	43.8	56	99.7	93.9	518	17	23.5	−0.07	3.63	0.01	22.9

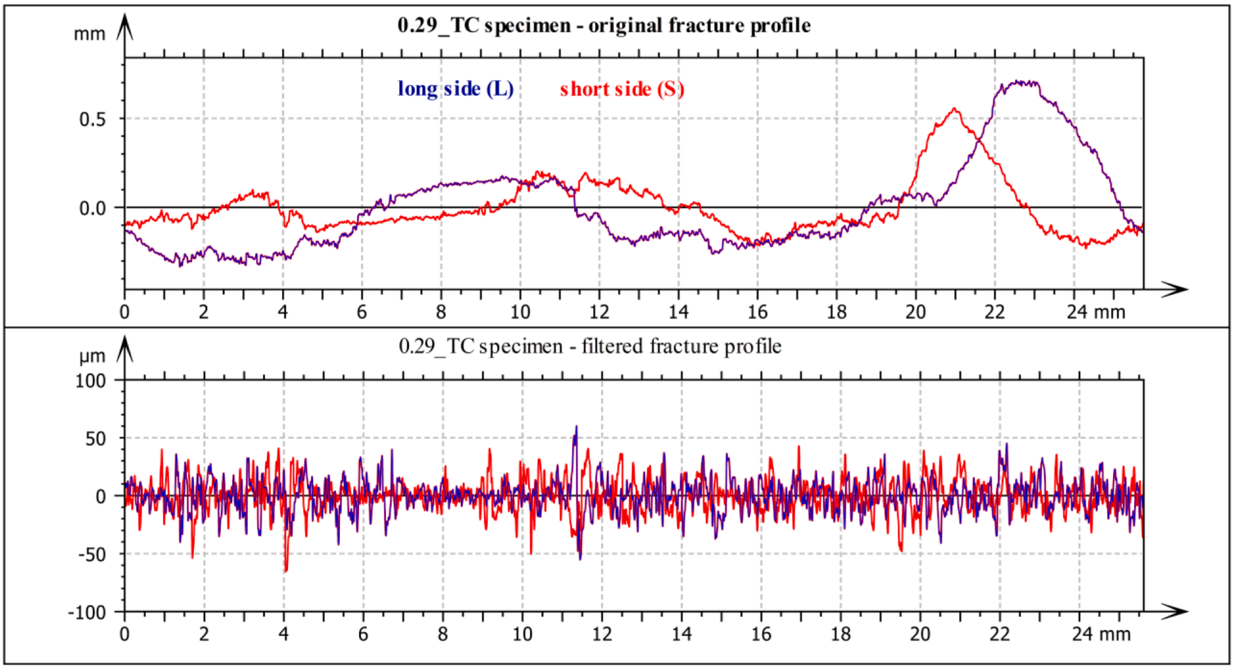

Fig. 6. Original profiles and result of filtering for both sides of 0.29_TC specimen.

4.2. An attempt to retrace the fatigue damage history based on fracture parameter

Considering the high correlation of some of the fracture surface parameters with fatigue life, it is assumed that the fatigue damage history can be roughly retraced based on them [56,57]. By simple transformation of Eq. (3), the relationship between the fatigue life and the roughness parameter can be obtained. Fig. 9 presents a comparison of the experimental and retraced fatigue lives. Quite good compliance has been achieved. However, it should be further investigated if this method works for other loading levels and materials.

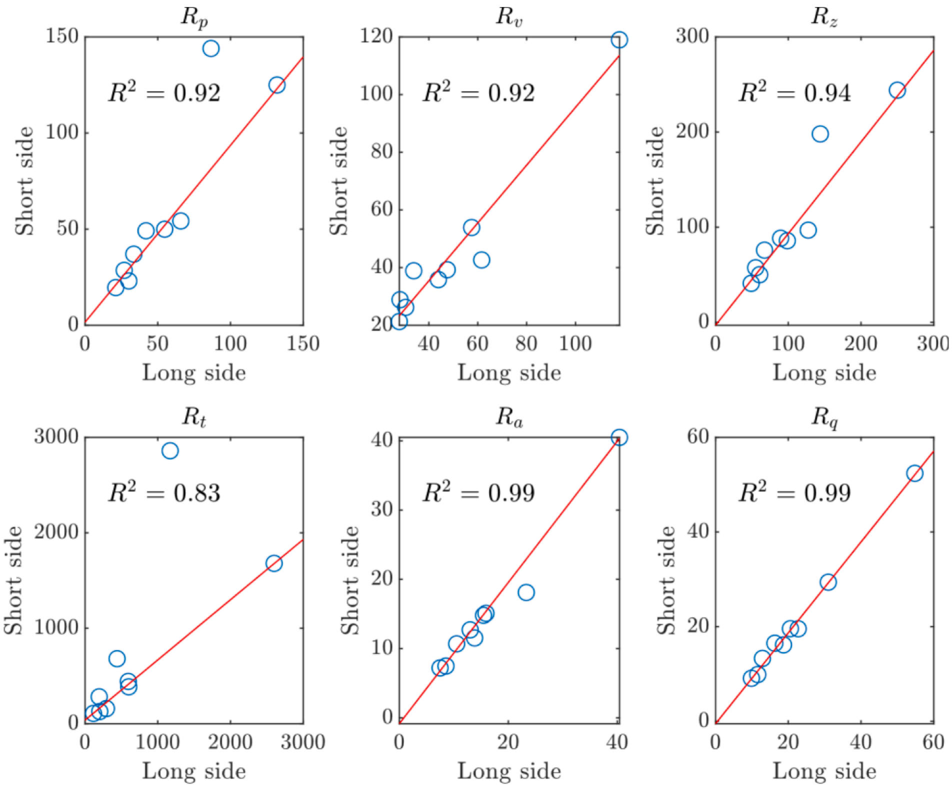

Fig. 7. Relationship of particular profile parameters evaluated for fracture of the long side (horizontal axis) and the short side (vertical axis): (a) R_p; (b) R_v; (c) R_z; (d) R_c; (e) R_t; (f) R_a; (g) R_q; (h) R_{sk}; (i) R_{ku}; (j) R_{mr}; and (k) R_{dc}. L denotes the long side and S denotes the short side.

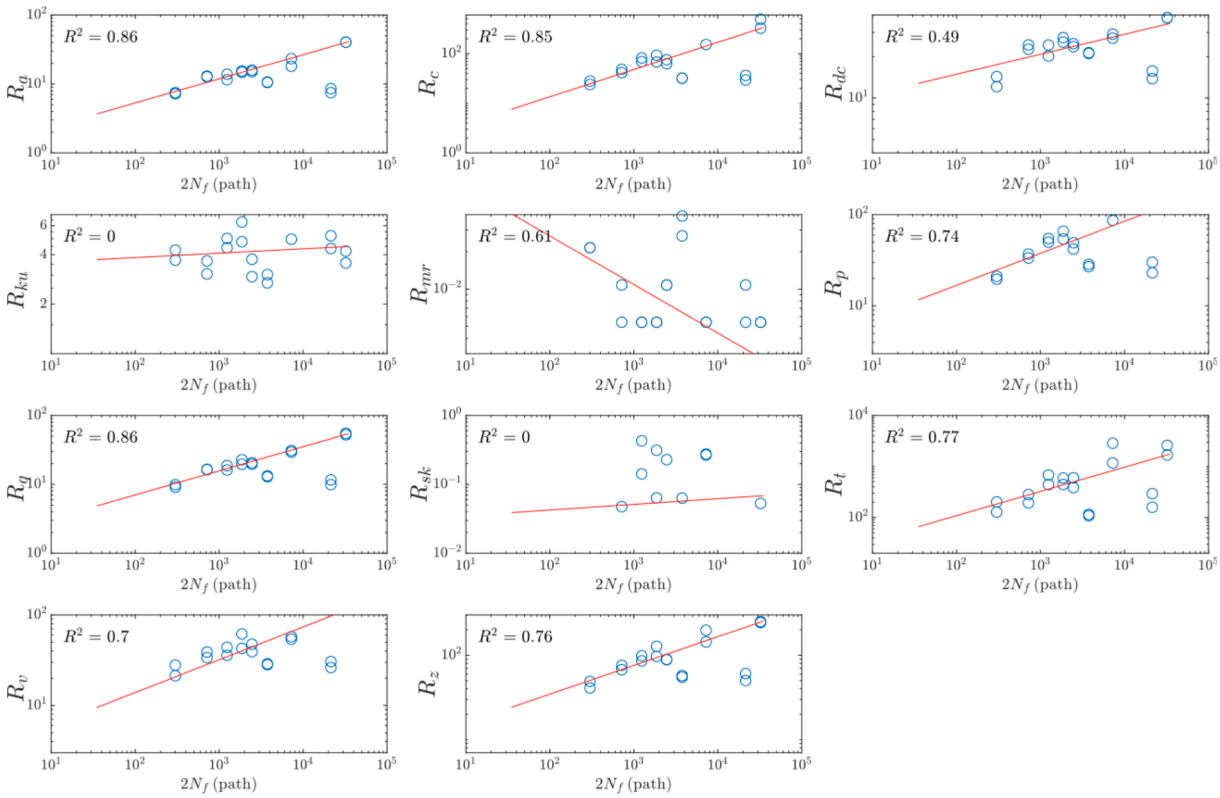

Fig. 8. Profile parameters versus fatigue life.

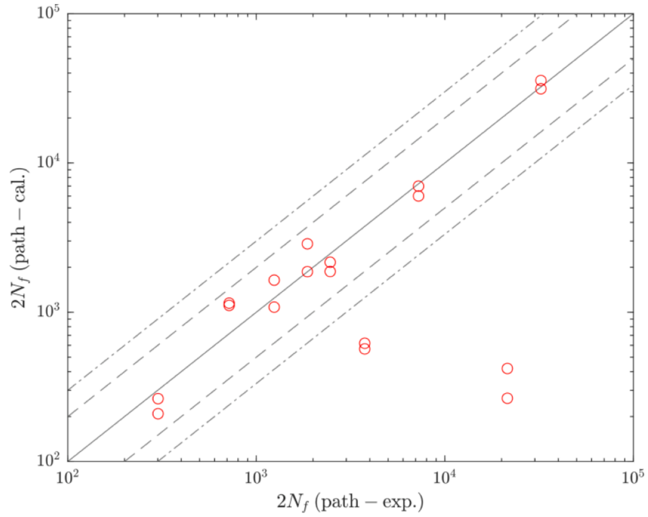

Fig. 9. A comparison of test versus retraced (calculated) fatigue life.

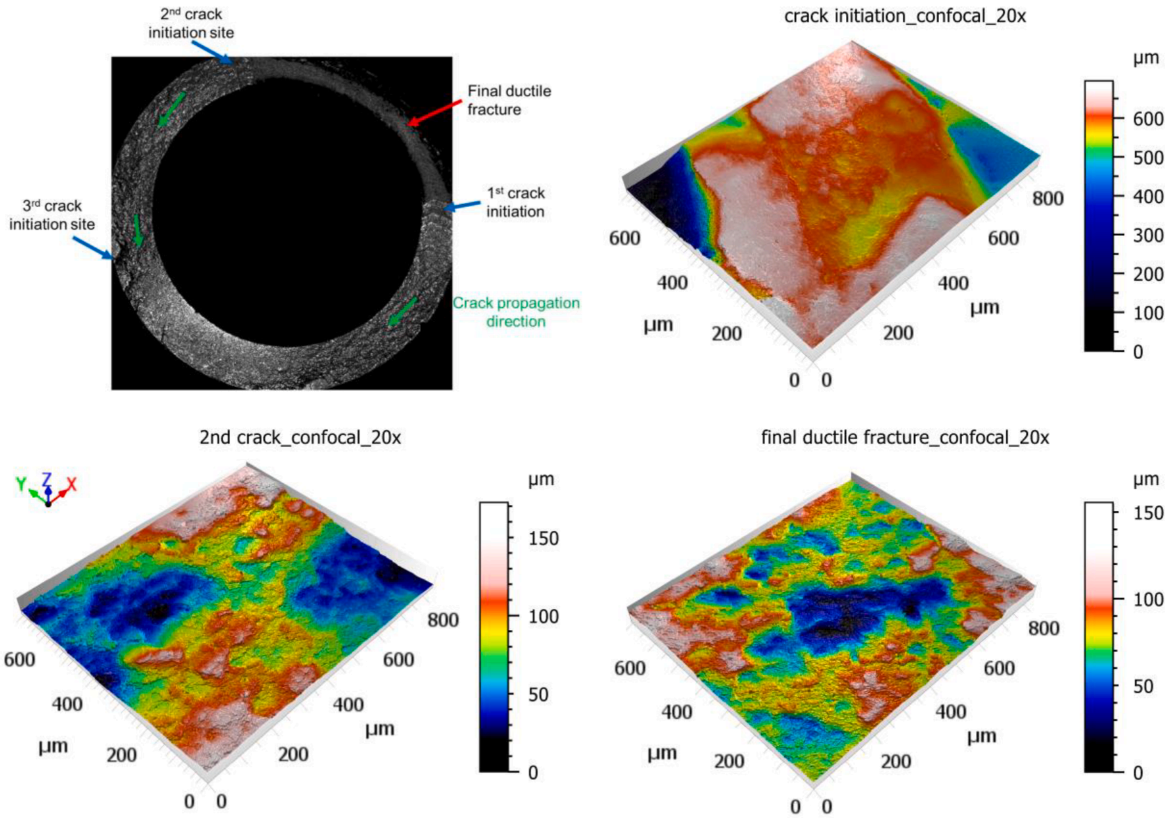

Fig. 10. Characteristic zones of selected fatigue fractures.

4.3. Fractographic analysis

Figs. 10 and 11 show characteristic images of the fatigue fracture surface features in terms of initiation and final ductile fracture zones obtained with both confocal and SEM shows, respectively. These areas were previously identified with FRASTA method [50]. Fig. 11 demonstrates the micrographs taken with a Tescan Vega 4 microscope for the zones in Fig. 10 (upper-left corner).

The failure process is characterized by the initiation of two cracks, nucleated from the surface of the specimen, in different regions of the outer surface (Fig. 10). As can be seen in the pseudo-color views, the images of both initiation sites are relatively similar in terms

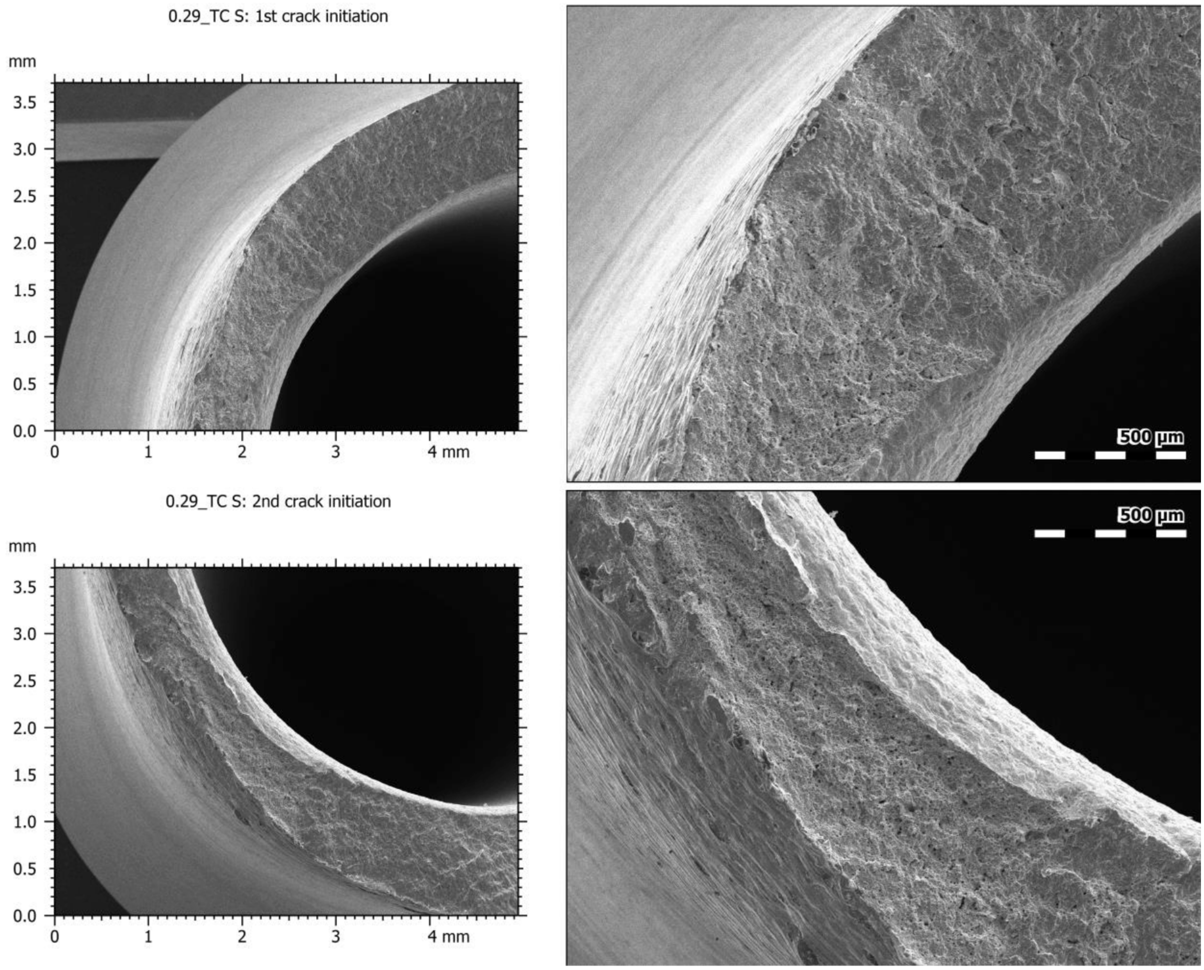

Fig. 11. SEM fractography for three different specimens shows crack initiation and final ductile fracture zones.

of surface topology features. On the contrary, for the final rupture area, the profiles are different, and the roughness is higher which can be explained by the higher fatigue crack growth rates.

Fig. 11 shows that the material exhibited the typical mechanisms associated to fatigue loading, such as traces of plastic deformation and ductility with evidence of microvoids (see black points in Fig. 11). It is also visible, particularly in the fatigue crack initiation regions, some river patterns with radial convergence to the initiation sites as well as the presence of secondary cracks of variable length. In the final rupture region, the pictures reveal more tortuous paths which are caused by the higher fatigue crack growth rates at this stage of propagation.

5. Conclusions

The post-failure fracture surface behavior of thin-walled tubular X5CrNi18-10 austenitic steel specimens subjected to asynchronous axial-torsional fatigue loading has been herein investigated. Pure axial and pure torsional loading were analyzed to better understand the effect of multiaxiality on facture surface topology parameters. It was found that the loading path significantly affects the surface topography. Thanks to this, it is possible to read from it how a given element has been damaged. On the other hand, it also allows the development of a model for determining the fatigue life of materials subjected to multiaxial asynchronous loading based on the fracture surface parameters, which is an important outcome. There is one additional benefit from implementing this method, the ability to read the fracture mechanisms. In more detail, the results of the present study suggest the following:

- The analysis of the fracture topography parameters, especially R_q, based on the profiles over the entire fracture surface, demonstrated that their values increase with higher values of the fatigue life N_f;
- The fracture surface topology parameters collected from both sides of the same specimen led to comparable results which reinforces the applicability of the proposed approach;

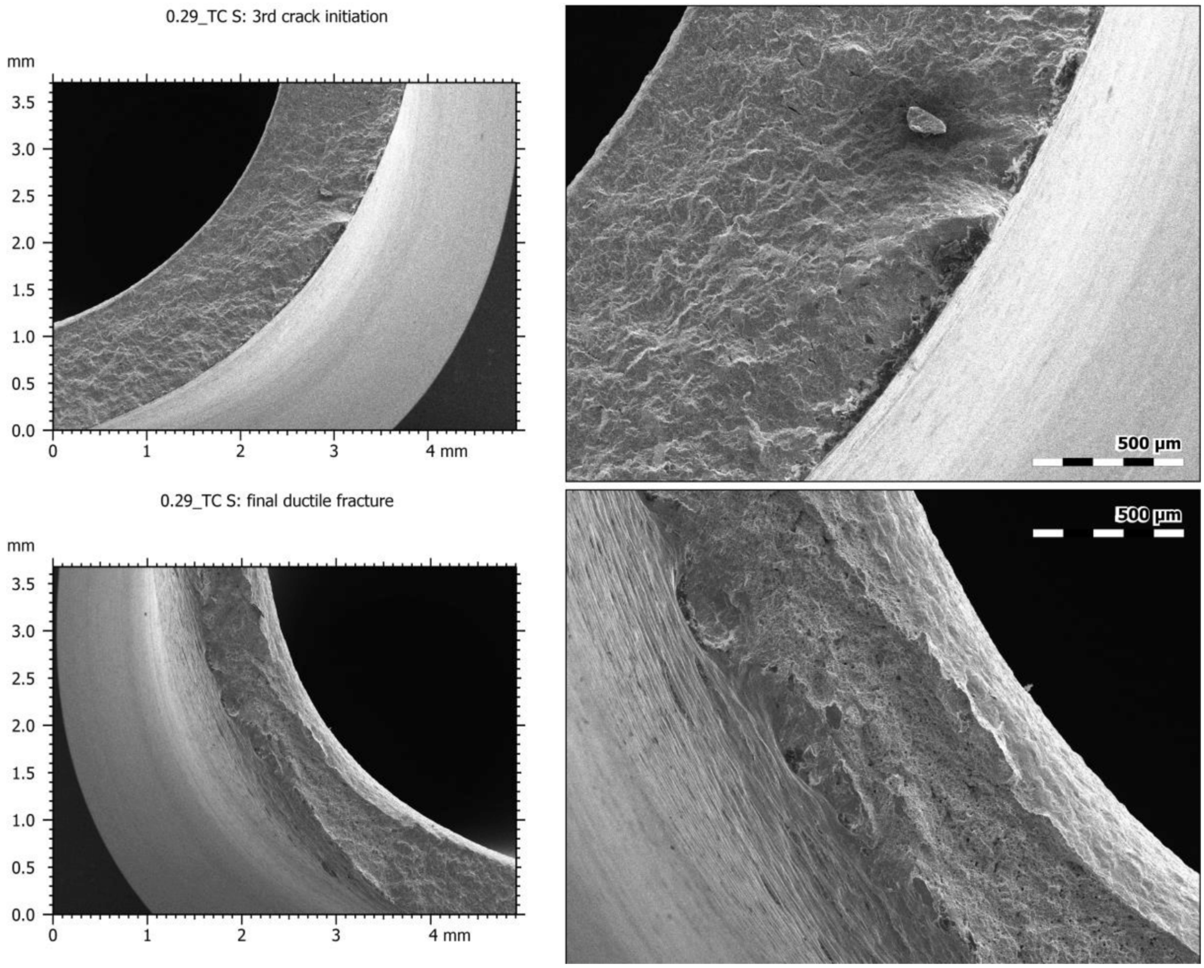

Fig. 11. (*continued*).

– The proposed fatigue damage model based on the R_q parameter was capable to estimate the fatigue life for the tested multiaxial asynchronous loading cases with a quite good compliance;
– The fractographic analysis of characteristic zones associated with the fatigue phenomenon showed differences failure mechanisms in the initiation region and the propagation region.

Declaration of Competing Interest

The authors declare that they have no known competing financial interests or personal relationships that could have appeared to influence the work reported in this paper.

Acknowledgements

The surface topography data were processed using the Mountains® software courtesy of Digital Surf, France.

Appendix A

Original profiles for both sides of each specimen are presented in Fig. A1. The letters “L” and “S” in the descriptions indicate the “long” and the “short” side of the broken specimen, respectively. The extracted profiles are provided below the isometric views of the fracture surface of each both broken part of the specimens for comparison.

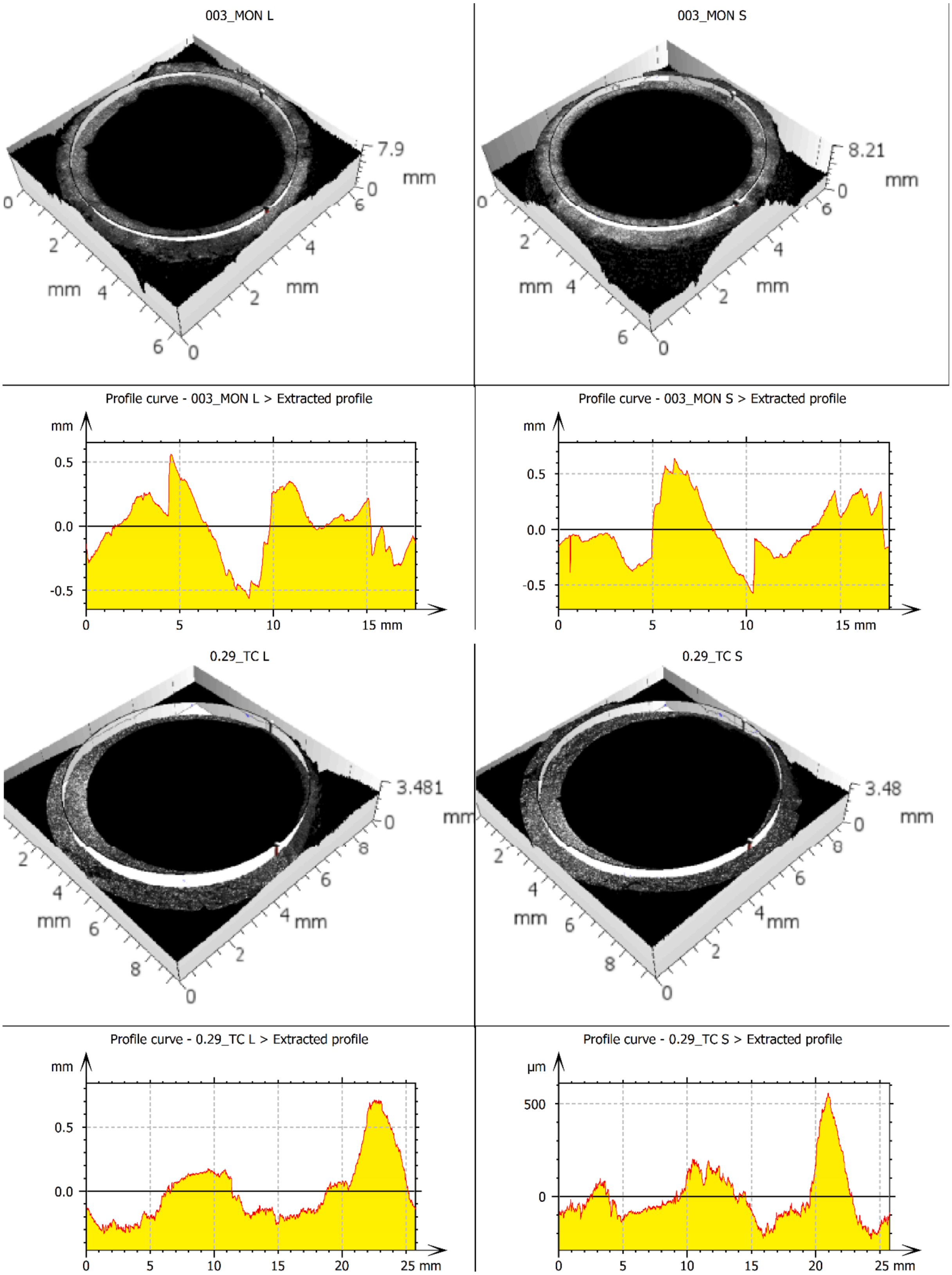

Fig. A1. Original profiles for both sides of each specimen.

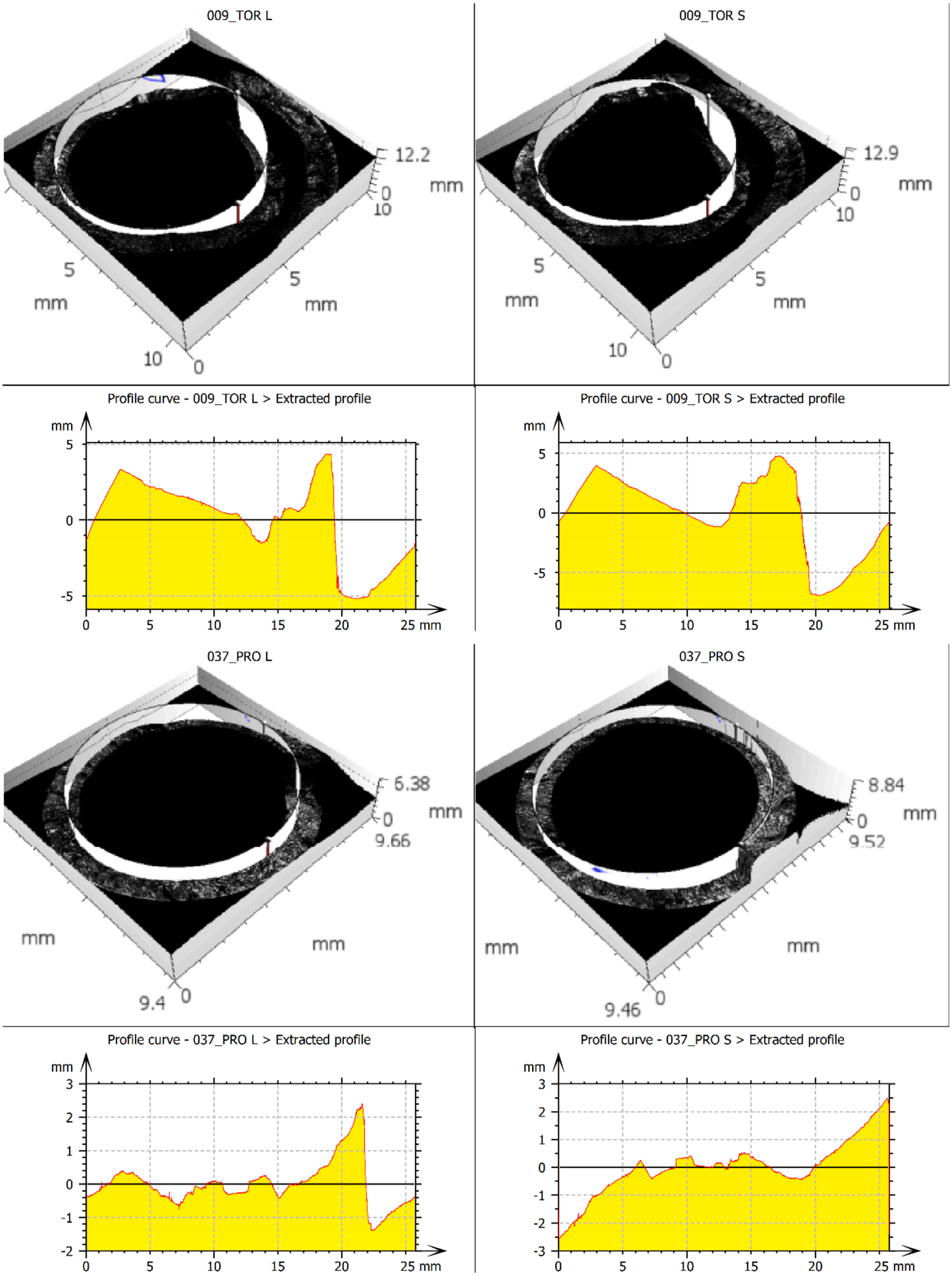

Fig. A1. (*continued*).

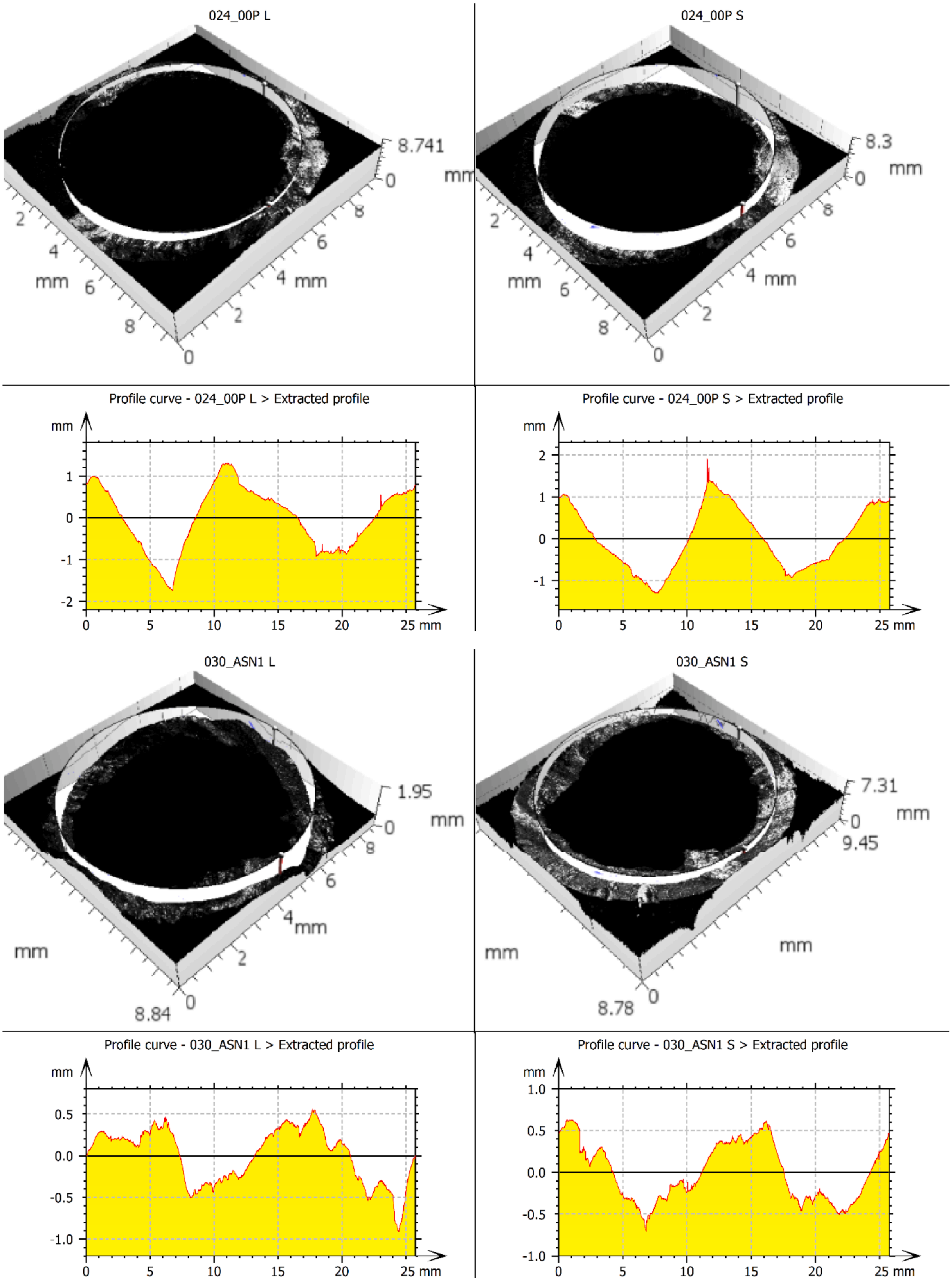

Fig. A1. (*continued*).

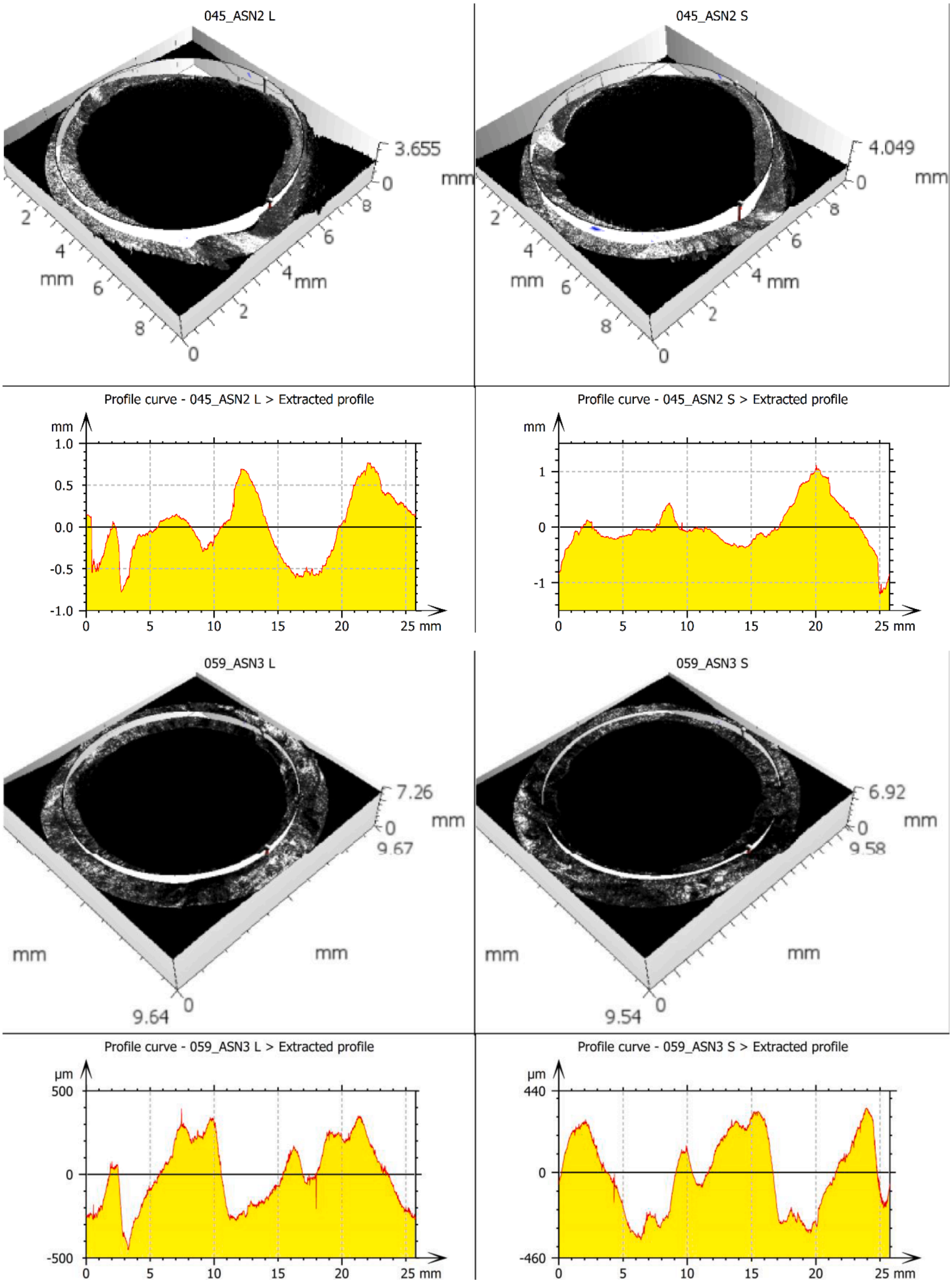

Fig. A1. (*continued*).

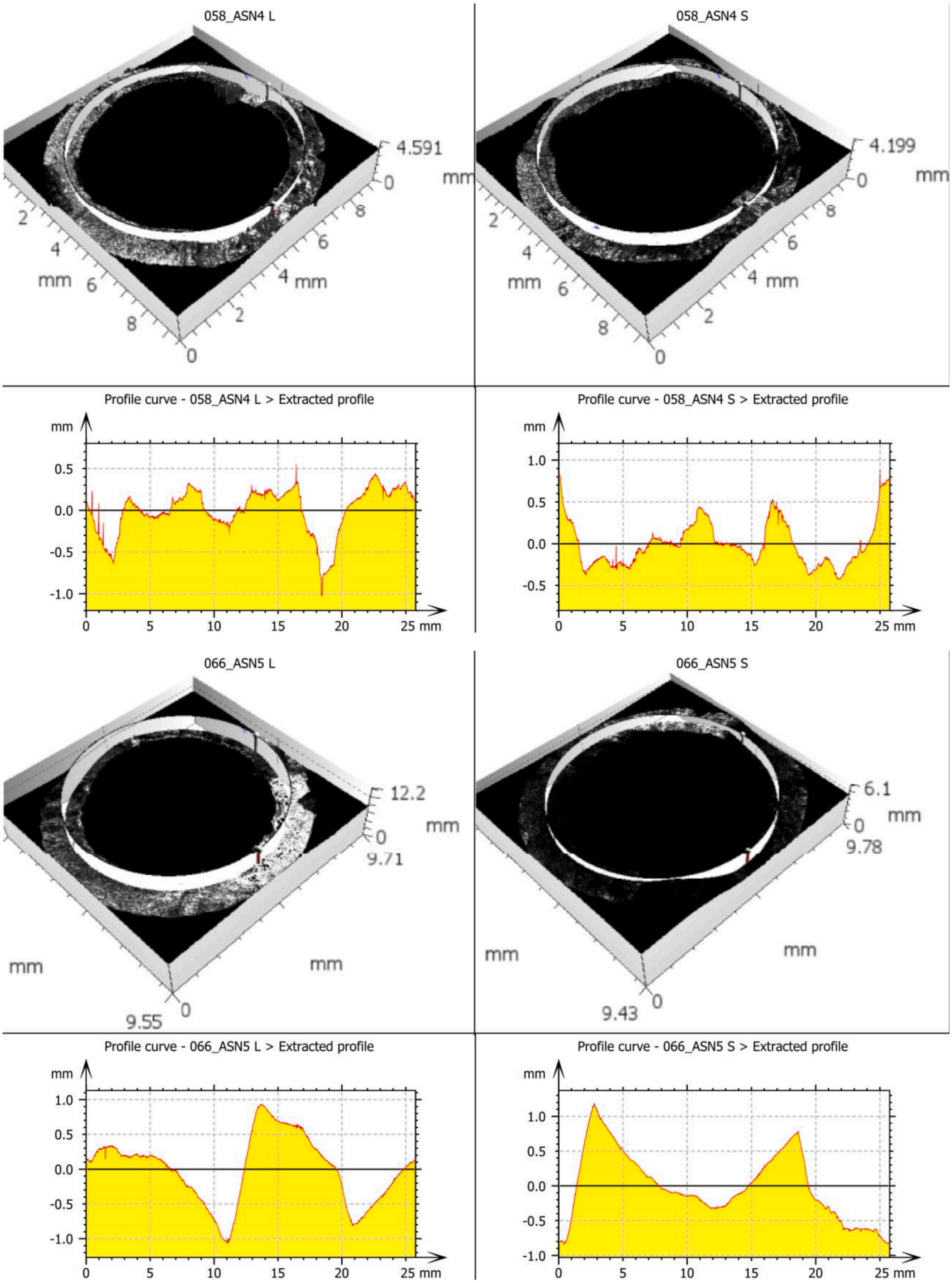

Fig. A1. (*continued*).

References

[1] Y. Zheng, X. Chen, Z. Zhang, S. Shi, G. Chen, B. Li, Multiaxial low cycle fatigue behavior and life prediction method of 316LN stainless steel at 550 °C, Int. J. Fatigue 156 (2022), 106637, https://doi.org/10.1016/j.ijfatigue.2021.106637.

[2] Y. Wang, W. Wang, L. Susmel, Constant/variable amplitude multiaxial notch fatigue of additively manufactured AISI 316L, Int. J. Fatigue 152 (2021), 106412, https://doi.org/10.1016/J.IJFATIGUE.2021.106412.

[3] R. Molaei, A. Fatemi, N. Phan, Multiaxial fatigue of LB-PBF additive manufactured 17–4 PH stainless steel including the effects of surface roughness and HIP treatment and comparisons with the wrought alloy, Int. J. Fatigue 137 (2020), 105646, https://doi.org/10.1016/j.ijfatigue.2020.105646.

[4] M. Kamaya, Y. Kitsunai, M. Koshiishi, True stress-strain curve acquisition for irradiated stainless steel including the range exceeding necking strain, J. Nucl. Mater. 465 (2015) 316–325, https://doi.org/10.1016/j.jnucmat.2015.05.027.

[5] P. Fernández-Pisón, J.A. Rodríguez-Martínez, E. García-Tabarés, I. Avilés-Santillana, S. Sgobba, Flow and fracture of austenitic stainless steels at cryogenic temperatures, Eng. Fract. Mech. 258 (2021), 108042, https://doi.org/10.1016/j.engfracmech.2021.108042.

[6] G.G. Youn, Y.J. Kim, Y. Miura, A parameter for characterizing thermal aging effect on fracture toughness of GTAW of 316L stainless steel, Eng. Fract. Mech. 239 (2020), 107318, https://doi.org/10.1016/j.engfracmech.2020.107318.

[7] Arruda EM, Boyce MC. Evolution of Plastic Anisotropy in Amorphous Polymers during Finite Straining. vol. 9. 1991. Doi: 10.1007/978-94-011-3644-0_112.

[8] F.V. Antunes, M.S.C. Ferreira, R. Branco, P. Prates, C. Gardin, C. Sarrazin-Baudoux, Fatigue crack growth versus plastic CTOD in the 304L stainless steel, Eng. Fract. Mech. 214 (2019) 487–503, https://doi.org/10.1016/j.engfracmech.2019.04.013.

[9] N. Nagaishi, M. Yoshikawa, S. Okazaki, J. Yamabe, F. Yoshida, H. Matsunaga, Evaluation of fatigue life and fatigue limit of circumferentially-notched Type 304 stainless steel in air and hydrogen gas based on crack-growth property and cyclic stress-strain response, Eng. Fract. Mech. 215 (2019) 164–177, https://doi.org/10.1016/j.engfracmech.2019.05.005.

[10] D. Rozumek, Z. Marciniak, G. Lesiuk, J.A. Correia, A.M.P. de Jesus, Experimental and numerical investigation of mixed mode I + II and I + III fatigue crack growth in S355J0 steel, Int. J. Fatigue 113 (2018) 160–170, https://doi.org/10.1016/J.IJFATIGUE.2018.04.005.

[11] J. Li, Y. Qiu, A path-dependent multiaxial fatigue life estimation criterion for metals under various loading conditions, Int. J. Fatigue 149 (2021), 106300, https://doi.org/10.1016/j.ijfatigue.2021.106300.

[12] M. Mehdizadeh, M.M. Khonsari, On the application of fracture fatigue entropy to multiaxial loading, Int. J. Fatigue 150 (2021), 106321, https://doi.org/10.1016/j.ijfatigue.2021.106321.

[13] G. Lesiuk, B. Rymsza, J. Rabiega, J.A.F.O. Correia, A.M.P. De Jesus, R. Calcada, Influence of loading direction on the static and fatigue fracture properties of the long term operated metallic materials, Eng. Fail. Anal. 96 (2019) 409–425, https://doi.org/10.1016/j.engfailanal.2018.11.007.

[14] Y. Chen, P. Xu, C. Liu, F. Wang, H. Song, Multiaxial fatigue behavior and life prediction of 7075–T651 aluminum alloy under two-step loading, Eng. Fract. Mech. 230 (2020), 107007, https://doi.org/10.1016/j.engfracmech.2020.107007.

[15] T. Liu, X. Qi, X. Shi, T. Zhang, G. Zhang, J. Zhang, Crack growth path of 30CrMnSiA steel under variable amplitude multiaxial loading, Int. J. Fatigue 153 (2021), 106502, https://doi.org/10.1016/j.ijfatigue.2021.106502.

[16] D. Rigon, F. Berto, G. Meneghetti, Estimating the multiaxial fatigue behaviour of C45 steel specimens by using the energy dissipation, Int. J. Fatigue 151 (2021), 106381, https://doi.org/10.1016/j.ijfatigue.2021.106381.

[17] J.A.F.O. Correia, P.J. Huffman, A.M.P. De Jesus, G. Lesiuk, J.M. Castro, R.A.B. Calcada, F. Bertod, Probabilistic fatigue crack initiation and propagation fields using the strain energy density, Strength Mater. 50 (4) (2018) 620–635, https://doi.org/10.1007/s11223-018-0007-5.

[18] A. Carpinteri, C. Ronchei, D. Scorza, S. Vantadori, Fracture mechanics based approach to fatigue analysis of welded joints, Eng. Fail. Anal. 49 (2015) 67–78, https://doi.org/10.1016/J.ENGFAILANAL.2014.12.021.

[19] A. Karolczuk, M. Słoński, Application of the Gaussian process for fatigue life prediction under multiaxial loading, Mech. Syst. Sig. Process. 167 (2022), 108599, https://doi.org/10.1016/j.ymssp.2021.108599.

[20] M.A. Meggiolaro, J.T.P. de Castro, A deviatoric tensile-based critical plane model to predict peak/mean normal stress effects in multiaxial fatigue, Int. J. Fatigue 155 (2022), 106615, https://doi.org/10.1016/j.ijfatigue.2021.106615.

[21] J. Liu, Y. Ran, Y. Wei, Z. Zhang, A critical plane-based multiaxial fatigue life prediction method considering the material sensitivity and the shear stress, Int. J. Press. Vessels Pip. 194 (2021), 104532, https://doi.org/10.1016/J.IJPVP.2021.104532.

[22] J. Papuga, A. Kaľavský, M. Lutovinov, I. Vízková, S. Parma, M. Nesládek, Evaluation of data sets usable for validating multiaxial fatigue strength criteria, Int. J. Fatigue 145 (2021), 106093, https://doi.org/10.1016/J.IJFATIGUE.2020.106093.

[23] R. Branco, J.D. Costa, L.P. Borrego, F. Berto, S.M.J. Razavi, W. Macek, Comparison of different one-parameter damage laws and local stress-strain approaches in multiaxial fatigue life assessment of notched components, Int. J. Fatigue 151 (2021), 106405, https://doi.org/10.1016/J.IJFATIGUE.2021.106405.

[24] A. Karolczuk, K. Kluger, T. Palin-Luc, Fatigue failure probability estimation of the 7075–T651 aluminum alloy under multiaxial loading based on the life-dependent material parameters concept, Int. J. Fatigue 147 (2021), 106174, https://doi.org/10.1016/j.ijfatigue.2021.106174.

[25] T.H. Ma, N. Gao, L. Chang, X.H. He, C.Y. Zhou, Low-cycle fatigue behavior and life prediction of CP-Ti under non-proportional and multiaxial loading, Eng. Fract. Mech. 254 (2021), 107930, https://doi.org/10.1016/j.engfracmech.2021.107930.

[26] D.H. Li, D.G. Shang, L. Xue, M.E. Barkey, H. Chen, Real-time damage evaluation method for multiaxial thermo-mechanical fatigue under variable amplitude loading, Eng. Fract. Mech. 229 (2020), 106948, https://doi.org/10.1016/J.ENGFRACMECH.2020.106948.

[27] L. Xu, T. Kojima, T. Itoh, Creep–fatigue life evaluation of type 304 stainless steel under non-proportional loading, Int. J. Press. Vessels Pip. 194 (2021), 104515, https://doi.org/10.1016/J.IJPVP.2021.104515.

[28] A. Nourian-Avval, M.M. Khonsari, A new model for fatigue life prediction under multiaxial loadings based on energy dissipation, Int. J. Fatigue 151 (2021), 106255, https://doi.org/10.1016/j.ijfatigue.2021.106255.

[29] A. Nourian-Avval, A. Fatemi, Fatigue performance and life prediction of cast aluminum under axial, torsion, and multiaxial loadings, Theor. Appl. Fract. Mech. 111 (2021), 102842, https://doi.org/10.1016/J.TAFMEC.2020.102842.

[30] Q. Han, P. Wang, Y. Lu, Path-dependent multiaxial fatigue prediction of welded joints using structural strain method, Fatigue Fract. Eng. Mater. Struct. 44 (2021) 2800–2826, https://doi.org/10.1111/ffe.13550.

[31] M. Bartošák, J. Horváth, M. Španiel, Multiaxial low-cycle thermo-mechanical fatigue of a low-alloy martensitic steel: Cyclic mechanical behaviour, damage mechanisms and life prediction, Int. J. Fatigue 151 (2021), 106383, https://doi.org/10.1016/j.ijfatigue.2021.106383.

[32] J. Albinmousa, M.J. Adinoyi, N. Merah, Multiaxial low-cycle-fatigue of stainless steel 410 alloy under proportional and non-proportional loading, Int. J. Press. Vessels Pip. 192 (2021), 104393, https://doi.org/10.1016/j.ijpvp.2021.104393.

[33] J. Kraft, M. Vormwald, Energy driven integration of incremental notch stress-strain approximation for multiaxial cyclic loading, Int. J. Fatigue 145 (2021), 106043, https://doi.org/10.1016/j.ijfatigue.2020.106043.

[34] Ł. Pejkowski, D. Skibicki, Stress-strain response and fatigue life of four metallic materials under asynchronous loadings: Experimental observations, Int. J. Fatigue 128 (2019), 105202, https://doi.org/10.1016/j.ijfatigue.2019.105202.

[35] Ł. Pejkowski, J. Seyda, Fatigue of four metallic materials under asynchronous loadings : Small cracks observation and fatigue life prediction, Int. J. Fatigue 142 (2021), 105904, https://doi.org/10.1016/j.ijfatigue.2020.105904.

[36] P. Arora, S.K. Gupta, M.K. Samal, J. Chattopadhyay, Validating generality of recently developed critical plane model for fatigue life assessments using multiaxial test database on seventeen different materials, Fatigue Fract. Eng. Mater. Struct. 43 (2020) 1327–1352, https://doi.org/10.1111/ffe.13169.

[37] P. Arora, S.K. Gupta, M.K. Samal, J. Chattopadhyay, Multiaxial fatigue experiments under variable strain paths and asynchronous loading and assessment of fatigue life using critical plane models, Int. J. Fatigue 145 (2020), 106049, https://doi.org/10.1016/j.ijfatigue.2020.106049.

[38] T. Liu, X. Qi, X. Shi, L. Gao, T. Zhang, J. Zhang, Effect of Loading Frequency Ratio on Multiaxial Asynchronous Fatigue Failure of 30CrMnSiA Steel, Materials 14 (2021) 3968, https://doi.org/10.3390/ma14143968.

[39] J. Papuga, M. Margetin, V. Chmelko, Various parameters of the multiaxial variable amplitude loading and their effect on fatigue life and fatigue life computation, Fatigue Fract. Eng. Mater. Struct. 44 (2021) 2890–2912, https://doi.org/10.1111/ffe.13560.
[40] S.P. Lynch, S. Moutsos, A brief history of fractography, J. Fail. Anal. Prev. 6 (6) (2006) 54–69.
[41] D.B. Garcia, A.F. Grandt, Fractographic investigation of fretting fatigue cracks in Ti-6Al-4V, Eng. Fail. Anal. 12 (4) (2005) 537–548.
[42] S.M. Taheri Mousavi, N. Richart, C. Wolff, J.F. Molinari, Dynamic crack propagation in a heterogeneous ceramic microstructure, insights from a cohesive model, Acta Mater. 88 (2015) 136–146, https://doi.org/10.1016/J.ACTAMAT.2015.01.003.
[43] A. Falkowska, A. Seweryn, Fatigue life of 316L steel sinters of varying porosity under conditions of uniaxial periodically variable loading at a fixed stress amplitude, Int. J. Fatigue 117 (2018) 496–510, https://doi.org/10.1016/j.ijfatigue.2018.07.025.
[44] S. Dutta, A. Karmakar, H. Roy, K. Barat, Automatic estimation of mechanical properties from fractographs using optimal anisotropic diffusion and Voronoi tessellation, Measurement 134 (2019) 574–585, https://doi.org/10.1016/J.MEASUREMENT.2018.10.100.
[45] C.R.F. Azevedo, R.R. Maia, E.A. Ariza, A.P. Tschiptschin, Failure analysis of a martensitic stainless steel (CA-15M) roll manufactured by centrifugal casting. Part I: Material and fractographic characterization, Eng. Fail. Anal. 36 (2014) 343–352, https://doi.org/10.1016/J.ENGFAILANAL.2013.10.020.
[46] M. Kowal, M. Szala, Diagnosis of the microstructural and mechanical properties of over century-old steel railway bridge components, Eng. Fail. Anal. 110 (2020), 104447, https://doi.org/10.1016/J.ENGFAILANAL.2020.104447.
[47] D. Martelo, D. Sampath, A. Monici, R. Morana, R. Akid, Correlative analysis of digital imaging, acoustic emission, and fracture surface topography on hydrogen assisted cracking in Ni-alloy 625+, Eng. Fract. Mech. 221 (2019), 106678 https://doi.org/10.1016/J.ENGFRACMECH.2019.106678.
[48] W. Macek, G. Robak, K. Żak, R. Branco, Fracture surface topography investigation and fatigue life assessment of notched austenitic steel specimens, Eng. Fail. Anal. 135 (2022), 106121, https://doi.org/10.1016/j.engfailanal.2022.106121.
[49] T. Vojtek, J. Pokluda, A. Hohenwarter, R. Pippan, Three-dimensional morphology of fracture surfaces generated by modes II and III fatigue loading in ferrite and austenite, Eng. Fract. Mech. 108 (2013) 285–293, https://doi.org/10.1016/J.ENGFRACMECH.2013.02.022.
[50] W. Macek, D. Sampath, Ł. Pejkowski, K. Żak, A brief note on monotonic and fatigue fracture events investigation of thin-walled tubular austenitic steel specimens via fracture surface topography analysis (FRASTA), Eng. Fail. Anal. 134 (2022), 106048, https://doi.org/10.1016/J.ENGFAILANAL.2022.106048.
[51] H.R. Jhansale, T.H. Topper, in: Cyclic Stress-Strain Behavior—Analysis, Experimentation, and Failure Prediction, ASTM International, 100 Barr Harbor Drive, PO Box C700, West Conshohocken, PA 19428-2959, 1971, pp. 246–246-25.
[52] F. Ellyin, K. Golos, Z. Xia, In-Phase and Out-of-Phase Multiaxial Fatigue, J. Eng. Mater. Technol. 113 (1991) 112, https://doi.org/10.1177/089124168601500202.
[53] ISO 4287. Geometrical Product Specifications (GPS) – Surface texture: Profile method – Terms, definitions and surface texture parameters. International Organization for Standardization 1997:25.
[54] K. Zak, Cutting mechanics and surface finish for turning with differently shaped CBN tools, Archive of Mechanical Engineering 64 (2017) 347–357, https://doi.org/10.1515/MECENG-2017-0021.
[55] M. Bartoszuk, Approximately Model of the Maximum Temperature on the Chip Surface, Materials 2021, Vol. 14, Page 2592. 14 (2021) 2592. Doi: 10.3390/MA14102592.
[56] A. Masoudi, M. Davarpanah Jazi, M. Mohrekesh, N.R. Masoudi, An investigation of rail failure due to wear using statistical pattern recognition techniques, Eng. Fail. Anal. 134 (2022), 106084, https://doi.org/10.1016/J.ENGFAILANAL.2022.106084.
[57] H.R. Ghanbari, M. Shariati, E. Sanati, N.R. Masoudi, Effects of spot welded parameters on fatigue behavior of ferrite-martensite dual-phase steel and hybrid joints, Eng. Fail. Anal. 134 (2022), 106079, https://doi.org/10.1016/J.ENGFAILANAL.2022.106079.